

# Self-Gravitational Force Calculation of Infinitesimally Thin Gaseous Disks on Nested Grids

Hsiang-Hsu Wang<sup>1</sup>, Ronald E. Taam<sup>1,3</sup>, David C. C. Yen<sup>3</sup>

yen@math.fju.edu.tw

## ABSTRACT

We extend the work of [Yen et al. \(2012\)](#) and develop 2nd order formulae to accommodate a nested grid discretization for the direct self-gravitational force calculation for infinitesimally thin gaseous disks. This approach uses a two-dimensional kernel derived for infinitesimally thin disks and is free of artificial boundary conditions. The self-gravitational force calculation is presented in generalized convolution forms for a nested grid configuration. A numerical technique derived from a fast Fourier transform is employed to reduce the computational complexity to be nearly linear. By comparing with analytic potential-density pairs associated with the generalized Maclaurin disks, the extended approach is verified to be of second order accuracy using numerical simulations. The proposed method is accurate, computationally fast and has the potential to be applied to the studies of planetary migration and the gaseous morphology of disk galaxies.

*Subject headings:* self-gravitating force, nested grid, infinitesimally thin disk, kernel

## 1. Introduction

As a direct consequence of the conservation of angular momentum and efficient radiative cooling, thin disks form naturally in the Universe. The substructures associated with barred and spiral galaxies, massive stars forming along spiral arms as well as the existence of central

---

<sup>1</sup>Institute of Astronomy and Astrophysics, Academia Sinica, P.O. Box 23-141, Taipei 10617, Taiwan, R.O.C.

<sup>2</sup>Department of Mathematics, Fu Jen Catholic University, New Taipei City, Taiwan.

<sup>3</sup>Department of Physics and Astronomy, Northwestern University, 2131 Tech Drive, Evanston, IL 60208, USA

starburst rings manifest that the self-gravity of gas is important to the evolution of disk galaxies (Lin et al. 2013; Seo & Kim 2014; Elmegreen et al. 2014; Kim et al. 2012; Lee & Shu 2012; Lee 2014). The self-gravity also plays a role in shaping planetary systems during the formation of planets (Inutsuka et al. 2010; Zhang et al. 2014). Hydrodynamic simulations including the effect of the disk’s self-gravity have been used to investigate the orbital evolution of a Jovian planet as reported in Zhang et al. (2008). The simulations show that the self-gravity of gas in an infinitesimally thin disk plays a significant role in the radial drift associated with the type III migration. The self-gravitational calculation used in Zhang et al. (2008) is based on a uniformly discretized Cartesian grid, and the method has been described in Yen et al. (2012). Since the self-gravity of gas within the Roche lobe of a protoplanet may influence the planetary migration as well as the mass accretion onto the protoplanet, it is highly desirable to perform global simulations with refined grids concentrated around the protoplanet.

The adequacy of numerical techniques for solving the self-gravity of the gas can be ascertained starting from the gravitational potential  $\Phi$  associated with the mass density,  $\rho$ , in three dimensional space, which can be represented by

$$\nabla \cdot (\nabla\Phi)(x, y, z) = 4\pi G\rho(x, y, z),$$

where  $\nabla = (\frac{\partial}{\partial x}, \frac{\partial}{\partial y}, \frac{\partial}{\partial z})$  or by the volume integral

$$\Phi(x, y, z) = G \iiint \frac{-\rho(\bar{x}, \bar{y}, \bar{z})}{\sqrt{(\bar{x} - x)^2 + (\bar{y} - y)^2 + (\bar{z} - z)^2}} d\bar{x} d\bar{y} d\bar{z},$$

where  $G$  is the gravitational constant. We are interested in the calculation for an infinitesimally thin disk, where the corresponding volumetric mass density  $\rho$  is associated with a surface density  $\sigma$ ,

$$\rho(x, y, z) = \sigma(x, y)\delta(z), \tag{1}$$

where  $\delta$  is the Dirac symbol. Thus, the problem is to solve the potential  $\Phi$  induced from a surface density,  $\sigma$ , contained in an infinitesimally thin layer,  $\Omega$ , satisfying the Poisson equation,

$$\nabla \cdot (\nabla\Phi)(x, y, z) = 4\pi G\sigma(x, y)\delta(z), \quad (x, y) \text{ in } \Omega. \tag{2}$$

The potential in the mid-plane,  $\Phi(x, y, 0)$ , is associated with a kernel integral via

$$\Phi(x, y, 0) = G \iint_{\Omega} \frac{-\sigma(\bar{x}, \bar{y})}{\sqrt{(x - \bar{x})^2 + (y - \bar{y})^2}} d\bar{x} d\bar{y}. \tag{3}$$

For simplicity, we set  $G = 1$  hereafter. We note that solving (2) is essentially a three-dimensional (3D) problem, while the integral form (3) involves only two-dimensional (2D) calculations when focusing only on the forces in the mid-plane.

Numerous methods have been proposed for three-dimensional potential calculations (Matsumoto & Hanawa 2003; Wackers 2005; McCorquodale et al. 2007; Greengard & Rokhlin 1987; Anderson 1986; Hockney & Eastwood 1981; Brandt 1977; Smith et al. 2004) including the Fast Multipole Method (FMM), the Method of Local Corrections (MLC), and FFT-based methods, multigrid, and domain decomposition. If one chooses to solve (2) using a fast algorithm for the 3D problem, one may reach at best a linear computational complexity of  $O(N^3)$ , where  $N$  is the number of zones in one direction. In contrast, solving the integral form (3) may have a computational complexity of only  $O(N^2)$ . In other words, solving (3) can be more computationally economical than solving (2). However, it seems more straightforward to develop a numerical method for a nested grid configuration for the differential form (2) than that for the integral form (3), since the differentiation operator involves only the local information. We note that the multigrid relaxation method is fast, flexible and has been used extensively when mesh refinements are required (Hockney & Eastwood 1981). However, the multigrid methods, which are by nature only for three-dimensional problems, cannot be reduced to two-dimensional calculations for an infinitesimally thin disk as discussed in this paper.

A few methods in the literature can be applied to solve the potential induced from an infinitesimally thin disk. The direct  $N$ -body method is conceptionally simple and relatively straightforward to implement, but it has only first order accuracy and high numerical complexity. The fast Fourier transform based methods have better numerical complexity, but are subject to periodic or isolated boundary conditions (James 1977). Its application is restricted to a calculation domain that is uniformly discretized. The spectral methods are popular and can solve (2) with better accuracy, however, artificial boundary conditions need to be specified before the calculations. The development of this subject has been recently reviewed by Shen & Wang (2009). In contrast to those aforementioned works, a direct method for gravitational force calculation has been developed in Yen et al. (2012). The method has a numerical complexity of  $O(N^2 \log(N))$ , with a numerical accuracy of second order and without the requirement of artificial boundary conditions. The major objective of this work is to develop the formulae and generalize the work of Yen et al. (2012) to accommodate the nested grid configuration.

The rest of this paper is organized as follows. In Section 2, we describe the proposed method using a direct integral via the Green’s function method. The main concept of the numerical calculations is to recast the calculation of (3) into a generalized convolution form.

In Section 3, a few examples with analytic solutions generalized from [Schulz \(2009\)](#) are adopted to verify the order of accuracy and the performance of the method. We discuss and conclude this work in the last section.

## 2. Method

The central idea underlying our approach is to solve for the gravitational force, rather than the potential, by taking a derivative of the integral expression for the potential, which is an integral over the surface density convoluted by the (3D) Green’s function of the Laplacian. As this integral would, in general, be difficult to calculate, approximations are required for **simplification**. The approximations rely on a discretised domain, and a truncated Taylor expansion of the surface density. For instance, the surface density is approximated by a linear function of  $(x, y)$  within a cell and the approximation follows that the accuracy is of second order. The integrals (in  $x$  and  $y$ ) can be evaluated within each cell using integrals of closed form and the force within a cell can be calculated. These forces can then be summed over cells of all patches and all levels in order to find the total forces. The numerical complexity of a direct calculation is  $O(N^4)$ , where  $N$  is the number of cells in one dimension. These forces can be represented in a discretized convolution form and the complexity is linear and reduced to  $O(N^2)$  with the help of FFT. In general, FFTs in a non-uniform grid present difficulties. In order to have the nested grid formulation be amenable to a FFT approach, one must determine the convolution forms for cells in differing patches, which is done in this work.

The proposed method has two parts. In the first part, we develop the formulae that can be used to approximate the integral (3) with second order accuracy. In particular, these formulae are expressed in a generalized convolution form, which can be applied to nested grid configurations. We note that using the fast Fourier transform for a non-uniformly discretized calculation domain is not straightforward. However, we demonstrate in the second part, how the fast Fourier transform can be applied to nested grid structures, so that the numerical complexity remains as  $O(N^2 \ln N)$  and the use of artificial boundary conditions is avoided.

### 2.1. Approximation of second order accuracy

Define the nested domains  $\Omega_k^\ell = [L_k^\ell, R_k^\ell] \times [B_k^\ell, T_k^\ell]$  for  $\ell = \ell_{\min}, \ell_{\min} + 1, \dots, \ell_{\max}$  and  $k = 1, 2, \dots, K^\ell$ , where  $\ell_{\min}$ ,  $\ell_{\max}$  and  $K^\ell$  are positive integers. Here,  $\ell$  denotes the level of grid and  $K^\ell$  represents the number of patch for a given level  $\ell$ . That is, there are  $\ell_{\max} - \ell_{\min} + 1$

grid levels and  $K^\ell$  patches for the grid level  $\ell$ . The domains  $\Omega_k^\ell$  for  $\ell = \ell_{\min}, \ell_{\min} + 1, \dots, \ell_{\max}$  and  $k = 1, 2, \dots, K^\ell$  are non-overlapping except at their boundaries. The cell size used to discretize the domain  $\Omega_k^\ell$  is uniform and described by  $(\frac{R_k^\ell - L_k^\ell}{N_k^\ell - 1}) \times (\frac{T_k^\ell - B_k^\ell}{M_k^\ell - 1}) := \Delta x_\ell \times \Delta y_\ell$ , where  $N_k^\ell - 1$  and  $M_k^\ell - 1$  are positive integers, corresponding to the number of cells in  $x$  and  $y$  directions, respectively. We note that all the patches of the same grid level  $\ell$  share the same cell size. We further denote the cells of  $\Omega_k^\ell$  as  $\Omega_{k,i,j}^\ell = \{(x, y) : x_{k,i}^\ell \leq x \leq x_{k,i+1}^\ell, y_{k,j}^\ell \leq y \leq y_{k,j+1}^\ell\}$ , where  $i = 0, 1, \dots, N_k^\ell - 1$  and  $j = 0, 1, \dots, M_k^\ell - 1$ . Here,  $x_{k,i}^\ell = i(R_k^\ell - L_k^\ell)/N_k^\ell + L_k^\ell = i(\Delta x)^\ell + L_k^\ell$  and  $y_{k,j}^\ell = j(T_k^\ell - B_k^\ell)/M_k^\ell + B_k^\ell = j(\Delta y)^\ell + B_k^\ell$ .

The computational domain  $\Omega$  is the set  $\bigcup_{\ell=\ell_{\min}}^{\ell_{\max}} \bigcup_{k=0}^{K^\ell} \Omega_k^\ell$ . Since the interiors of patches  $\Omega_k^\ell$  are mutually exclusive, except at the boundaries of the patches, every point in the calculation domain  $\Omega$  can only belong to one specific patch.

By (3), the potential induced from the surface density  $\sigma$  is rewritten as

$$\Phi(x, y, 0) = \iint K(\bar{x} - x, \bar{y} - y, 0) \sigma(\bar{x}, \bar{y}) d\bar{x} d\bar{y}, \quad (4)$$

where  $K(x, y, z) = \frac{-1}{\sqrt{x^2 + y^2 + z^2}}$  is the Green's function of the Laplacian equation in the entire three dimension space. The  $x$ -force is associated with the partial derivative in the  $x$ -direction of the potential defined in (4),

$$\begin{aligned} -\frac{\partial}{\partial x} \Phi(x, y, 0) &= -\iint \frac{\partial}{\partial x} K(\bar{x} - x, \bar{y} - y, 0) \sigma(\bar{x}, \bar{y}) d\bar{x} d\bar{y} \\ &= \sum_{\ell=\ell_{\min}}^{\ell_{\max}} \sum_{k=1}^{K^\ell} -\iint_{\Omega_k^\ell} \frac{\partial}{\partial x} K(\bar{x} - x, \bar{y} - y, 0) \sigma(\bar{x}, \bar{y}) d\bar{x} d\bar{y}. \end{aligned} \quad (5)$$

where  $\frac{\partial}{\partial x} K(x, y, z) = \frac{x}{(x^2 + y^2 + z^2)^{3/2}}$  is the partial derivative in  $x$ -direction of the Green's function  $K$ . Assuming that the surface density  $\sigma$  contained in the bounded domain  $\Omega$  is sufficiently smooth, the Taylor expansion of  $\sigma(\bar{x}, \bar{y})$  on  $\Omega_{k,i,j}^\ell$  is represented as

$$\sigma(\bar{x}, \bar{y}) \simeq \sigma_{k,i,j}^\ell + \delta_{k,i,j}^{\ell,x} (\bar{x} - x_{k,i+1/2}^\ell) + \delta_{k,i,j}^{\ell,y} (\bar{y} - y_{k,j+1/2}^\ell), \quad (6)$$

where  $\sigma_{k,i,j}^\ell$ ,  $\delta_{k,i,j}^{\ell,x}$  and  $\delta_{k,i,j}^{\ell,y}$  are constants in the cell  $\Omega_{k,i,j}^\ell$ . Substituting (6) into (5), the  $x$ -force can be approximated by

$$\begin{aligned} -\frac{\partial}{\partial x} \Phi(x, y, 0) &\simeq \sum_{\ell=\ell_{\min}}^{\ell_{\max}} \sum_{k=1}^{K^\ell} \sum_{i=0}^{N_k^\ell-1} \sum_{j=0}^{M_k^\ell-1} -\iint_{\Omega_{k,i,j}^\ell} \frac{\partial}{\partial x} K(\bar{x} - x, \bar{y} - y, 0) \times \\ &\quad \left[ \sigma_{k,i,j}^\ell + \delta_{k,i,j}^{\ell,x} (\bar{x} - x_{k,i+1/2}^\ell) + \delta_{k,i,j}^{\ell,y} (\bar{y} - y_{k,j+1/2}^\ell) \right] d\bar{x} d\bar{y}. \end{aligned}$$

Furthermore, the  $x$ -force at the cell center  $(x, y) = (x_{\hat{k}, \hat{i}+1/2}^\ell, y_{\hat{k}, \hat{j}+1/2}^\ell)$  of  $\Omega_{\hat{k}, \hat{i}, \hat{j}}^\ell$  is

$$\begin{aligned} -\frac{\partial}{\partial x} \Phi(x_{\hat{k}, \hat{i}+1/2}^\ell, y_{\hat{k}, \hat{j}+1/2}^\ell, 0) &\simeq \sum_{\ell=\ell_{\min}}^{\ell_{\max}} \sum_{k=1}^{K^\ell} \sum_{i=0}^{i_k^\ell} \sum_{j=0}^{j_k^\ell} - \iint_{\Omega_{k,i,j}^\ell} \frac{\partial}{\partial x} K(\bar{x} - x_{\hat{k}, \hat{i}+1/2}^\ell, \bar{y} - y_{\hat{k}, \hat{j}+1/2}^\ell, 0) \times \\ &\quad \left[ \sigma_{k,i,j}^\ell + \delta_{k,i,j}^{\ell,x} (\bar{x} - x_{\hat{k}, \hat{i}+1/2}^\ell) + \delta_{k,i,j}^{\ell,y} (\bar{y} - y_{\hat{k}, \hat{j}+1/2}^\ell) \right] d\bar{x}d\bar{y} \\ &\equiv F^{x,0} + F^{x,x} + F^{x,y}. \end{aligned}$$

Thus,

$$\begin{aligned} F^{x,0} &\equiv - \sum_{\ell=\ell_{\min}}^{\ell_{\max}} \sum_{k=1}^{K^\ell} \sum_{i=0}^{N_k^\ell-1} \sum_{j=0}^{M_k^\ell-1} \sigma_{k,i,j}^\ell \iint_{\Omega_{k,i,j}^\ell} \frac{\partial}{\partial x} K(\bar{x} - x_{\hat{k}, \hat{i}+1/2}^\ell, \bar{y} - y_{\hat{k}, \hat{j}+1/2}^\ell, 0) d\bar{x}d\bar{y} \\ &= - \sum_{\ell=\ell_{\min}}^{\ell_{\max}} \sum_{k=1}^{K^\ell} \sum_{i=0}^{N_k^\ell-1} \sum_{j=0}^{M_k^\ell-1} \sigma_{k,i,j}^\ell \int_{y_{k,j}^\ell}^{y_{k,j+1}^\ell} \int_{x_{k,i}^\ell}^{x_{k,i+1}^\ell} \frac{\partial}{\partial x} K(\bar{x} - x_{\hat{k}, \hat{i}+1/2}^\ell, \bar{y} - y_{\hat{k}, \hat{j}+1/2}^\ell, 0) d\bar{x}d\bar{y} \\ &= \sum_{\ell=\ell_{\min}}^{\ell_{\max}} \sum_{k=1}^{K^\ell} \sum_{i=0}^{N_k^\ell-1} \sum_{j=0}^{M_k^\ell-1} \sigma_{k,i,j}^\ell \times \mathcal{K}^{x,0,\ell,\ell}(\bar{x} - x_{\hat{k}, \hat{i}+1/2}^\ell, \bar{y} - y_{\hat{k}, \hat{j}+1/2}^\ell) \Big|_{x_{k,i}^\ell}^{x_{k,i+1}^\ell} \Big|_{y_{k,j}^\ell}^{y_{k,j+1}^\ell}. \end{aligned}$$

where  $g(x)|_a^b = g(b) - g(a)$ , and the corresponding antiderivative of  $\frac{\partial}{\partial x} K(x, y, 0)$  is given by

$$\mathcal{K}^{x,0,\ell,\ell}(x, y) = -|\text{sgn}(x)| \ln(y + \sqrt{x^2 + y^2}) - (1 - |\text{sgn}(x)|) \text{sgn}(y) \ln(|y|). \quad (7)$$

The equation (7) is derived from

$$\int_c^d \int_a^b \frac{x}{(x^2 + y^2)^{3/2}} dx dy = \int_c^d -\frac{1}{\sqrt{x^2 + y^2}} \Big|_a^b dy.$$

For a nested grid calculation,  $a$  or  $b$  can be zero. In the case that  $ab \neq 0$ ,

$$\int_c^d -\frac{1}{\sqrt{b^2 + y^2}} dy = -\ln(y + \sqrt{b^2 + y^2}) \Big|_c^d, \quad (8)$$

otherwise,

$$\int_c^d -\frac{1}{|y|} dy = -\text{sgn}(y) \ln |y| \Big|_c^d. \quad (9)$$

Combining (8) and (9), (7) follows. Compared to Equation (3.11) in [Yen et al. \(2012\)](#), (7) is more general and suitable for a nested grid calculation. Similarly for  $F^{x,x}$  and  $F^{x,y}$ , which

are defined as

$$\begin{aligned}
 F^{x,x} &= \sum_{\ell=\ell_{\min}}^{\ell_{\max}} \sum_{k=1}^{K^\ell} \sum_{i=0}^{N_k^\ell-1} \sum_{j=0}^{M_k^\ell-1} \delta_{k,i,j}^{\ell,x} \times \mathcal{K}^{x,x,\ell,\hat{\ell}}(\bar{x} - x_{\hat{k},\hat{i}+1/2}^\ell, \bar{y} - y_{\hat{k},\hat{j}+1/2}^\ell) \Big|_{x_{k,i}^\ell}^{x_{k,i+1}^\ell} \Big|_{y_{k,j}^\ell}^{y_{k,j+1}^\ell}, \\
 F^{x,y} &= \sum_{\ell=\ell_{\min}}^{\ell_{\max}} \sum_{k=1}^{K^\ell} \sum_{i=0}^{N_k^\ell-1} \sum_{j=0}^{M_k^\ell-1} \delta_{k,i,j}^{\ell,y} \times \mathcal{K}^{x,y,\ell,\hat{\ell}}(\bar{x} - x_{\hat{k},\hat{i}+1/2}^\ell, \bar{y} - y_{\hat{k},\hat{j}+1/2}^\ell) \Big|_{x_{k,i}^\ell}^{x_{k,i+1}^\ell} \Big|_{y_{k,j}^\ell}^{y_{k,j+1}^\ell}.
 \end{aligned}$$

Here,

$$\begin{aligned}
 \mathcal{K}^{x,x,\ell,\hat{\ell}}(x, y) &= x\mathcal{K}^{x,0,\ell,\hat{\ell}}(x, y) - y \ln(x + \sqrt{x^2 + y^2}) \\
 \mathcal{K}^{x,y,\ell,\hat{\ell}}(x, y) &= y\mathcal{K}^{x,0,\ell,\hat{\ell}}(x, y) - \sqrt{x^2 + y^2}.
 \end{aligned}$$

We now show that the  $\mathcal{K}^{x,\cdot,\ell,\hat{\ell}}$  can be expressed in a generalized convolution form. Let us consider the representation of  $x_{k,i}^\ell - x_{\hat{k},\hat{i}+1/2}^\ell$  in

$$\mathcal{K}^{x,x,\ell,\hat{\ell}}(\bar{x} - x_{\hat{k},\hat{i}+1/2}^\ell, \bar{y} - y_{\hat{k},\hat{j}+1/2}^\ell) \Big|_{x_{k,i}^\ell}^{x_{k,i+1}^\ell} \Big|_{y_{k,j}^\ell}^{y_{k,j+1}^\ell}.$$

This calculation involves the following three cases:

Case 1. When  $\ell = \hat{\ell}$ , the term  $x_{k,i}^\ell - x_{\hat{k},\hat{i}+1/2}^\ell$  is equal to  $\Delta x_\ell(i - \hat{i} - 1/2) + (L_k^\ell - L_{\hat{k}}^\ell)$ .

Case 2. When  $\ell > \hat{\ell}$ , the term  $x_{k,i}^\ell - x_{\hat{k},\hat{i}+1/2}^\ell$  is equal to  $\Delta x_\ell(i - \frac{\Delta x_{\hat{\ell}}}{\Delta x_\ell}(\hat{i} + 1/2)) + (L_k^\ell - L_{\hat{k}}^\ell)$ .

Case 3. When  $\ell < \hat{\ell}$ , the term  $x_{k,i}^\ell - x_{\hat{k},\hat{i}+1/2}^\ell$  is equal to  $\Delta x_{\hat{\ell}}(\frac{\Delta x_\ell}{\Delta x_{\hat{\ell}}}i - \hat{i} - 1/2) + (L_k^\ell - L_{\hat{k}}^\ell)$ .

Now, we impose the condition that  $\Delta x_{\hat{\ell}}/\Delta x_\ell$  is a positive integer for  $\ell > \hat{\ell}$  and  $\Delta x_\ell/\Delta x_{\hat{\ell}}$  a positive integer for  $\hat{\ell} > \ell$ . We note that in Case 2, the  $x_{k,i}^\ell$  can be identical to  $x_{\hat{k},\hat{i}+1/2}^\ell$ . Similar discussion can be also applied to  $y_{k,j}^\ell - y_{\hat{k},\hat{j}+1/2}^\ell$ . In general, the calculation of  $F^{x,\cdot}$  involves the following convolution forms,

$$\begin{aligned}
 a_{\hat{n},\hat{p}} &= \sum_n \sum_p b_{\hat{n}-n,\hat{p}-p} c_{n,p}, \quad \text{for Case 1,} \\
 a_{\hat{n},\hat{p}} &= \sum_n \sum_p b_{m\hat{n}-n,q\hat{p}-p} c_{n,p}, \quad \text{for Case 2,} \\
 a_{\hat{n},\hat{p}} &= \sum_n \sum_p b_{\hat{n}-mn,\hat{p}-qp} c_{n,p}, \quad \text{for Case 3,}
 \end{aligned}$$

where  $m \equiv \frac{\Delta x_{\hat{\ell}}}{\Delta x_\ell}$ ,  $q \equiv \frac{\Delta y_{\hat{\ell}}}{\Delta y_\ell}$  for  $\ell > \hat{\ell}$  and  $m \equiv \frac{\Delta x_\ell}{\Delta x_{\hat{\ell}}}$ ,  $q \equiv \frac{\Delta y_\ell}{\Delta y_{\hat{\ell}}}$  for  $\ell < \hat{\ell}$ . The matrix  $b$  corresponds to the force kernels, while the matrix  $c$  corresponds to the surface density.

## 2.2. Fast calculation for a generalized convolution form

In this subsection, we calculate the generalized convolution forms in Cases 2 and 3 discussed in the previous subsection. For the sake of simplicity and clarity, only a calculation in one-dimension is demonstrated. Let  $\{a_n\}$ ,  $\{b_n\}$  and  $\{c_n\}$  be three sequences and define the generalized  $z$ -transform to be  $a(z; m, k) = \sum_n a_{mn+k} z^{mn+k}$ , where  $m$  is a positive integer and  $k$  is a non-negative integer. A similar definition of the  $z$ -transform is also applied for  $b(z; m, k)$  and  $c(z; m, k)$ . The calculation for a one-dimensional convolution problem is the following.

Case 1'.  $\ell = \hat{\ell}$ . In this case, the calculation of gravitational forces is known to be a normal convolution form which can be computed using a fast Fourier transform (see [Yen et al. \(2012\)](#)).

Case 2'.  $\ell > \hat{\ell}$ . The one-dimensional convolution is generalized to

$$a_n = \sum_{\hat{n}} b_{mn-\hat{n}} c_{\hat{n}}, \quad n \in \mathcal{Z}, \quad (10)$$

where  $m > 1$  is an integer. Now,

$$\begin{aligned} a(z^m; 1, 0) &= \sum_n a_n z^{mn} = \sum_n \sum_{k=0}^{m-1} \sum_{n'} b_{mn-mn'-k} c_{mn'+k} z^{mn} \\ &= \sum_{k=0}^{m-1} \sum_{n'} c_{mn'+k} z^{mn'+k} \sum_n b_{m(n-n')-k} z^{m(n-n')-k} \\ &= \sum_{k=0}^{m-1} b(z; m, -k) c(z; m, k) \end{aligned}$$

In this case, the coefficients  $\{a_n\}$  are a summation of the products of the transforms of  $\{b_{mn'+k}\}$  and  $\{c_{mn'+k}\}$  from  $k = 0$  up to  $k = m - 1$ . By applying the fast Fourier transform, the computational complexity is linearly proportional to the lengths of  $\{b_n\}$  and  $\{c_n\}$ . This one-dimensional calculation corresponds to computing the two-dimensional force at the center of  $\Omega_{\hat{k}, \hat{i}, \hat{j}}^{\hat{\ell}}$  contributed from the surface density on a finer cell denoted by  $\Omega_{k, i, j}^{\ell}$ .

Case 3'.  $\ell < \hat{\ell}$ . The one-dimensional convolution is generalized to

$$a_n = \sum_{\hat{n}} b_{n-m\hat{n}} c_{\hat{n}}, \quad n \in \mathcal{Z}, \quad (11)$$



where  $m > 1$  is an integer. Multiplying  $z^n$  from both sides of (11), it is

$$a_n z^n = \sum_{\hat{n}} b_{n-m\hat{n}} c_{\hat{n}} z^n,$$

and to rewrite  $n = mn' + k$ ,  $k = 0, 1, \dots, m - 1$  and  $n' \in \mathcal{Z}$ . For a given  $k$ , where  $k = 0, 1, \dots, m - 1$ , the coefficients  $\{a_{mn'+k} : n' \in \mathcal{Z}\}$  can be calculated by

$$\sum_{n'} a_{mn'+k} z^{mn'+k} = \sum_{\hat{n}} c_{\hat{n}} z^{m\hat{n}} \sum_{n'} b_{m(n'-\hat{n})+k} z^{m(n'-\hat{n})+k} = c(z^m; 1, 0) b(z; m, k).$$

In this case, since the sequence  $\{a_n\}$  is split into  $m$  groups, the calculation of the coefficients  $\{a_n\}$  requires  $m$  times Fourier transform. This one-dimensional calculation corresponds to computing the two-dimensional force at the center of  $\Omega_{\hat{k}, \hat{i}, \hat{j}}^{\ell}$  contributed from the surface density on a coarser cell denoted by  $\Omega_{k,i,j}^{\ell}$ .

We demonstrate an example for Case 2' and Case 3'. Let two vectors  $b$  and  $c$  be

$$b = (b_0, b_1, b_2, b_3, b_4, b_5, b_6, b_7), \quad c = (c_0, c_1, c_2, c_3).$$

For Case 2' and  $m = 2$ , the vector  $a$  defined in (10) is

$$\begin{aligned} a_0 &= b_0 c_0 \\ a_1 &= b_0 c_2 + b_1 c_1 + b_2 c_0 \\ a_2 &= b_1 c_3 + b_2 c_2 + b_3 c_1 + b_4 c_0 \\ a_3 &= b_3 c_3 + b_4 c_2 + b_5 c_1 + b_6 c_0 \\ a_4 &= b_5 c_3 + b_6 c_2 + b_7 c_1 \\ a_5 &= b_7 c_3 \end{aligned}$$

The generalized  $z$ -transform of the vector  $a$  is  $a_0 + a_1 z^2 + a_2 z^4 + a_3 z^6 + a_4 z^8 + a_5 z^{10}$ , which is identical to  $(b_0 + b_2 z^2 + b_4 z^4 + b_6 z^6)(c_0 + c_2 z^2) + (b_1 z + b_3 z^3 + b_5 z^5 + b_7 z^7)(c_1 z + c_3 z^3)$ .

For Case 3' and  $m = 2$ , the vector  $a$  defined in (11) is

$$\begin{aligned} a_0 &= b_0 c_0 & a_1 &= b_1 c_0 \\ a_2 &= b_0 c_1 + b_2 c_0 & a_3 &= b_1 c_1 + b_3 c_0 \\ a_4 &= b_0 c_2 + b_2 c_1 + b_4 c_0 & a_5 &= b_1 c_2 + b_3 c_1 + b_5 c_0 \\ a_6 &= b_0 c_3 + b_2 c_2 + b_4 c_1 + b_6 c_0 & a_7 &= b_1 c_3 + b_3 c_2 + b_5 c_1 + b_7 c_0 \\ a_8 &= b_2 c_3 + b_4 c_2 + b_6 c_1 & a_9 &= b_3 c_3 + b_5 c_2 + b_7 c_1 \\ a_{10} &= b_4 c_3 + b_6 c_2 & a_{11} &= b_5 c_3 + b_7 c_2 \\ a_{12} &= b_6 c_3 & a_{13} &= b_7 c_3 \end{aligned}$$

Due to  $m = 2$ , the coefficients of the coefficients of the vector  $a$  are split into two groups  $(a_0, a_2, a_4, a_6, a_8, a_{10}, a_{12})$  and  $(a_1, a_3, a_5, a_7, a_9, a_{11}, a_{13})$ , which can be calculated from the generalized  $z$ -transform

$$(b_0 + b_2z^2 + b_4z^4 + b_6z^6)(c_0 + c_1z^2 + c_2z^4 + c_3z^6), \text{ and } (b_1z + b_3z^3 + b_5z^5 + b_7z^7)(c_0 + c_1z^2 + c_2z^4 + c_3z^6),$$

respectively, and compared the results with the generalized  $z$ -transform of  $(a_{2k})$  and  $(a_{2k+1})$ , where  $k = 0, 1, 2, \dots, 6$ .

### 3. Results

Potential-density pairs of infinitesimally thin disks are adopted to explore the performance of the proposed method. The surface density, which is generalized from the disk model discussed in [Schulz \(2009\)](#), is described by

$$\sigma_{D_n}(r; \alpha) = \begin{cases} \sigma_0(1 - \frac{r^2}{\alpha^2})^{n-1/2}, & \text{for } r < \alpha, \\ 0, & \text{for } r \geq \alpha, \end{cases} \quad (12)$$

where  $r = \sqrt{x^2 + y^2}$ ,  $\sigma_0$  is the surface density at the disk center,  $\alpha$  is a prescribed constant, and  $n$  represents the order of the disk. The corresponding potential associated with a disk,  $\sigma_{D_n}$ , is described in Appendix A by a set of recursive formulae. Numerical results obtained from the proposed method are compared with the analytic solutions associated with  $\sigma_{D_5}$  disks and are presented below.

It is known that the complexity of the calculation of a convolution is nearly linear  $O(M \log M)$ , where  $M$  is the length of vectors. The numerical complexity of the proposed method is linear  $O(N)$  for the calculation of force kernel  $\mathcal{K}^{x, \cdot, \ell, \hat{\ell}}$ , where  $N$  is the total number of cells. It follows that the total complexity is nearly linear  $O(N \log N)$ . Thus, we focus on exploring the order of accuracy associated with the proposed method.

Let us define the  $p$ -norm of a function as

$$\|f\| = \left( \int_{\Omega} |f(x)|^p \right)^{1/p}, \quad \text{if } p \geq 1$$

and

$$\|f\| = \text{ess max}_{\Omega} |f(x)|, \quad \text{if } p = \infty.$$

The errors between the analytic and numerical solution for various resolutions using different norms ( $L^1$ ,  $L^2$  and  $L^\infty$ ) demonstrate different senses of convergence.  $L^1$  norm measures the

variation of errors.  $L^2$  error norm is often associated with the energy involved in the errors. For example, the integral of the square of the electric field  $\int E(x)^2 dx$ , i.e., the square of the  $L^2$  norm, is the energy stored in the electric field.  $L^\infty$  norm measures the errors in a pointwise sense which is a strong sense of convergence. We apply those definitions of norm to the following examples and show that the proposed method is of second order accuracy.

The common properties of the examples discussed below are summarized as follows: (1) The disk model  $\sigma_{D_5}$  with a specific  $\alpha$ , which describes the size of the disk, is adopted to construct either a monopole (examples 1, 2) or a dipole field (examples 3, 4) to demonstrate the order of accuracy of our algorithm. (2) The one-side cell size of those cells in  $\Omega_0^\ell$  is one-half of that in  $\Omega_0^{\ell-1}$ . That is, the cell size ratio used between levels  $\ell - 1$  and  $\ell$  is taken to be 2. (3) The cell size of  $\Omega_0^0$  is described by  $(\Delta x) = (\Delta y) = (1/2)^{k-1}$ , with  $k = 5, \dots, 10$ , corresponding to the one-side cell number  $N = 32, \dots, 1024$ . We note that the number of **cells**  $N$  is applied to the root level, i.e.,  $\ell = 0$ . The cells of all levels of refinement are half sized as  $N$  is doubled. (4) Figures 1 to 4 corresponds to Examples 1 to 4 described below. In each figure, the mesh configuration is schematically shown in the top-left panel, the top-right panel shows the contours of the surface density, and the contours of absolute errors for  $x$ -force and  $y$ -force between analytic and numerical solutions are shown in the bottom-left and bottom-right panels in the common logarithmic scale, respectively. (5) Tables 1 to 4 show the corresponding  $L^1$ ,  $L^2$ , and  $L^\infty$  errors between analytic and numerical solutions for  $k = 5, \dots, 10$ .

*Example 1.* We demonstrate the order of accuracy using a  $\sigma_{D_5}$  disk with  $\alpha = 0.85$ . The disk is centered at the origin of coordinates and covered with two levels of nested grids. The domains of the grids are the following:  $\Omega_0^1 = [-1/2, 1/2] \times [-1/2, 1/2]$ , and  $\Omega_0^0 = [-1, 1] \times [-1, 1] \cap (\Omega_0^1)^c$ . The corresponding errors between analytic and numerical solutions for  $x$ -force and  $r$ -force are detailed in Table 1. It shows that the proposed method is almost second order accuracy for each norm in this example.

*Example 2.* In this case, we show the nested grid calculation using three levels with  $\ell = 0, 1, 2$ . The surface density adopted is identical to that used in *Example 1*. The domains of the grids are the following:  $\Omega_0^2 = [-1/4, 1/4] \times [-1/4, 1/4]$ ,  $\Omega_0^1 = [-1/2, 1/2] \times [-1/2, 1/2] \cap (\Omega_0^2)^c$  and  $\Omega_0^0 = [-1, 1] \times [-1, 1] \cap (\Omega_0^2 \cup \Omega_0^1)^c$ . The corresponding errors between analytic and numerical solutions for  $x$ -force and  $r$ -force are detailed in Table 2. It shows that the proposed method is also almost second order accuracy for each norm in this example.

*Example 3.* The non-axisymmetric case consists of two  $\sigma_{D_5}$  disks with  $\alpha = \sqrt{2}/4$  and is demonstrated for a two-level nested grid simulation. The centers of two disks are located at  $(-1/2, 0)$  and  $(1/2, 0)$ . The domains of the grids are the following:  $\Omega_0^1 = [-0.75, -0.25] \times$

$[-0.25, 0.25]$ ,  $\Omega_1^1 = [0.25, 0.75] \times [-0.25, 0.25]$  and  $\Omega_0^0 = ([-1, 1] \times [-1, 1]) \cap (\Omega_0^1 \cup \Omega_1^1)^c$ . The corresponding errors between analytic and numerical solutions for  $x$ -force and  $y$ -force are detailed in Table 3. It shows that the order of accuracy is 2 for  $L^1$  and  $L^2$  norms, while 1.9 for  $L^\infty$  norm.

*Example 4.* The non-axisymmetric distribution of surface density is the same as that used in Example 3. In this case, the disks are covered with three-level nested grids. The domains of the grids are the following: For level  $\ell = 2$ ,  $\Omega_0^2 = [0.25, 0.75] \times [-0.25, 0.25]$  and  $\Omega_1^2 = [-0.75, -0.25] \times [-0.25, 0.25]$ ; for level  $\ell = 1$ ,  $\Omega_0^1 = [-0.9, -0.1] \times [-0.4, 0.4] \cap (\Omega_1^2)^c$  and  $\Omega_1^1 = [0.1, 0.9] \times [-0.4, 0.4] \cap (\Omega_0^2)^c$ ; and for  $\ell = 0$ ,  $\Omega_0^0 = [-1, 1] \times [-1, 1] \cap (\Omega_0^2 \cup \Omega_1^2 \cup \Omega_0^1 \cup \Omega_1^1)^c$ . The corresponding errors between analytic and numerical solutions for  $x$ -force and  $y$ -force are detailed in Table 4. It shows that the order of accuracy is 2 for  $L^1$  and  $L^2$  norms, while 1.9 for  $L^\infty$  norm.

#### 4. Conclusions and discussions

We have extended the method developed by Yen et al. (2012) for directly calculating the self-gravity force in an infinitesimally thin disk, i.e., in two dimensions, induced from a surface density on a nested grid configuration. It is worth noting that the direct approach is to represent the forces in a convolution form on uniform/nested grids. Therefore, the fast Fourier transform is employed only for speeding up the computational time or reducing the numerical complexity. The method also has been demonstrated to be of second order accuracy by an analytic potential-density pairs.

In practice, the implementation of the proposed method for (7) can be modified as

$$\mathcal{K}^{x,0,\ell,\hat{\ell}}(x, y) = -|\text{sgn}(x)| \ln(y + \sqrt{x^2 + y^2} + \epsilon) - (1 - |\text{sgn}(x)|) \text{sgn}(y) \ln(|y| + \epsilon), \quad (13)$$

where  $\epsilon$  is a positive number less than the round off errors. We note that the number  $\epsilon$  is only introduced in numerical calculations to avoid numerical Not-a-Number (NaN) errors. The value of  $\epsilon$  is of the order of the machine error and should not be taken as a softening length.

As shown in the bottom row of Figures 1 to 4, the major errors are concentrated in the immediate vicinity of the interfaces where the spatial resolution undergoes a transition. This degrades the order of accuracy to roughly 1.9 in terms of the  $L^\infty$  norm. This actually demonstrates the advantage of using the integral form (3), since the density distribution is treated smoothly when crossing the interface. Strong spurious forces at the boundaries would be visible if the mass enclosed within a cell is treated as a particle located at the cell center.

It is expected that the inclusion of mesh refinement will improve the numerical accuracy in comparison with the case without refinement, since more details are taken into account in the refined grids. To determine the benefit from mesh refinement, the errors within the domain defined by  $\Omega_0^1$  in *Example 1* are analyzed for  $N = 512$  with and without refinement. For this specific case, the improvement in terms of  $L^1$ ,  $L^2$  and  $L^\infty$  are 1.57, 1.58, -0.22, respectively. This means that the accuracy is overall significantly improved, but slightly degraded in a pointwise sense. We do not expect the overall improvement can be second order since only a portion of the disk is refined. The slightly negative value of  $L^\infty$  is also expected due to the presence of the interface between levels. This work, however, shows that the errors induced by the interface between levels dissipates at a speed of nearly second order as  $N$  increases.

In comparison with the work of Yen et al. (2012), a model using  $\sigma_{D_2}$  disk with other parameters identical to that of *Example 1* is explored. With  $\alpha = 0.85$ , the size of the disk is larger than the domain of refinement, i.e., only a part of the disk is refined. The corresponding error analyses are detailed in Table 5. Similar to the conclusions of Yen et al. (2012), the calculation with refinement shows almost second order accuracy in terms of  $L^1$  and  $L^2$  norms, while converges to an order  $\approx 1.5$  for  $L^\infty$  norm. However, a detailed comparison between Table 5 of this work and Table 1 of Yen et al. (2012) shows that the mesh refinement not only improves the numerical accuracy, it also somewhat improves the order of convergence. The reduction in  $L^\infty$  norm for a  $\sigma_{D_2}$  disk, i.e., the error in pointwise sense, is due to the singularity appearing in the second derivative of the density at the edge of the disk. This indicates that a  $\sigma_{D_2}$  by nature is not suitable for verifying a numerical method with an accuracy higher than first order. On the other hand, this also suggests the limitation of the algorithm developed in this work. The requirement of smoothness in the density distribution reduces the numerical accuracy at density discontinuities.

Discontinuities in density are fairly common in astrophysical environments and numerical applications. For a specific case, it is possible to improve the order of numerical accuracy around a discontinuity if the analytical form of the density is known a priori, for instance, replacing the Taylor expansion by a least square approach to minimize the error to a second order accuracy at a discontinuity. Unfortunately, in general, the density distribution is a quantity that needs to be calculated numerically and determining discontinuities is not a trivial task either. Furthermore, a Poisson solver is usually coupled with a (magneto-)hydrodynamical solver, which usually reduces the order of accuracy to zero order, i.e., in terms of  $L^\infty$ , around a discontinuity, improvements of both hydrodynamical and Poisson solvers are desirable in the future.

We believe that the nested grid calculation would also be of use for applications requiring

polar coordinates. Based on the Green’s function representation of the potential, [Chan et al. \(2006\)](#) employ a pseudo-spectral method on a scaled cosine radial grid to achieve the high order accuracy. A modification to a uniform polar grid [Li et al. \(2009\)](#) is developed for disks with vertical structures and the associated overall computational complexity is  $O(N_r N_\phi \log N_\phi + N_\phi N_r^2)$ , where  $N_r$  is the number of cells in the radial direction and  $N_\phi$  is the number of cells in the azimuthal direction. The method proposed here can be generalized to polar coordinates with second order accuracy and nearly linear complexity using the methods described in [Wang et al. \(2015\)](#).

The authors would like to acknowledge the support of the Theoretical Institute for Advanced Research in Astrophysics (TIARA) based in Academia Sinica Institute of Astronomy and Astrophysics (ASIAA). C. C. Yen is supported by Short-term Visiting Program for Domestic Scholars, Academia Sinica, Taiwan, under the Grant 104-2-1-08-22. Thanks to Mr. Sam Tseng for assistance on the computational facilities and resources (TIARA cluster). The authors thank the referee for comments that helped to improve the clarity and presentation of this paper.

## REFERENCES

- Anderson, C. R. 1986, [JCoPh](#), **62**, 111
- Brandt, A. 1977, [MaCom](#), **31**, 333
- Chan, C.-k., Psaltis, D., & Özel, F. 2006, [ApJ](#), **645**, 506
- Elmegreen, D. M., Elmegreen, B. G., Erroz-Ferrer, S., et al. 2014, [ApJ](#), **780**, 32
- Greengard, L., & Rokhlin, V. 1987, [JCoPh](#), **73**, 325
- Hockney, R. W., & Eastwood, J. W. 1981, *Computer Simulation Using Particles*
- Inutsuka, S.-i., Machida, M. N., & Matsumoto, T. 2010, [ApJ](#), **718**, L58
- James, R. A. 1977, [JCoPh](#), **25**, 71
- Kim, W.-T., Seo, W.-Y., & Kim, Y. 2012, [ApJ](#), **758**, 14
- Lee, W.-K. 2014, [ApJ](#), **792**, 122
- Lee, W.-K., & Shu, F. H. 2012, [ApJ](#), **756**, 45

- Li, S., Buoni, M. J., & Li, H. 2009, [ApJS](#), **181**, 244
- Lin, L.-H., Wang, H.-H., Hsieh, P.-Y., et al. 2013, [ApJ](#), **771**, 8
- Matsumoto, T., & Hanawa, T. 2003, [ApJ](#), **583**, 296
- McCorquodale, P., Colella, P., Balls, G. T., & Baden, S. B. 2007, *CAMCoS*, **2**, 57
- Schulz, E. 2009, [ApJ](#), **693**, 1310
- Seo, W.-Y., & Kim, W.-T. 2014, [ApJ](#), **792**, 47
- Shen, J., & Wang, L.-l. 2009, *CCoPh*, **5**, 195
- Smith, B. F., Bjørstad, P. E., & Gropp, W. D. 2004, *Domain decomposition : parallel multi-level methods for elliptic partial differential equations* (Cambridge: Cambridge University Press)
- Wackers, J. 2005, [JCoAM](#), **180**, 1
- Wang, H.-H., Yen, D. C. C., & Taam, R. E. 2015, [ApJS](#), **221**, 4
- Yen, C.-C., Taam, R. E., Yeh, K. H.-C., & Jea, K. C. 2012, [JCoPh](#), **231**, 8246
- Zhang, H., Liu, H.-G., Zhou, J.-L., & Wittenmyer, R. A. 2014, [RAA](#), **14**, 433
- Zhang, H., Yuan, C., Lin, D. N. C., & Yen, D. C. C. 2008, [ApJ](#), **676**, 639

### Appendix: Recursive formula for potential-density pairs of a family of finite disks

Potential-density pairs for a family of finite disks characterized by a surface density  $\Sigma_n = \sigma_0(1 - R^2/\alpha^2)^{n-1/2}$  is described. It is a generalization of the study for  $n = 0, 1, 2$  in [Schulz \(2009\)](#). The potential  $\Phi_{D_n}$  corresponds to the finite disks with surface density  $\Sigma_n$ . The potential  $\Phi_{D_1}$  is known as the Maclaurin potential for the Maclaurin disk

$$\Sigma_{\text{Mac}}(R; \alpha) = \begin{cases} \sigma_0 \sqrt{1 - R^2/\alpha^2} & \text{for } R < \alpha, \\ 0 & \text{for } R > \alpha. \end{cases}$$

It is represented for  $z = 0$  as

$$\begin{aligned}\Phi_{D_1}(R, 0; \alpha) &= \Phi_{\text{Mac}} = -\frac{\pi G \sigma_0}{2\alpha} \left[ (2\alpha^2 - R^2) \sin^{-1} \frac{\alpha}{R} + \alpha \sqrt{R^2 - \alpha^2} \right], \\ &= -\frac{\pi G \sigma_0}{2\alpha} R^2 \left[ (2(\xi^2 - 1) + 1) \sin^{-1} \xi + \xi \sqrt{1 - \xi^2} \right],\end{aligned}$$

for  $R \geq \alpha$ , where  $\xi = \alpha/R$  and

$$\Phi_{D_1}(R, 0; \alpha) = -\frac{\pi^2 \sigma_0 G}{4\alpha} (2\alpha^2 - R^2),$$

for  $R \leq \alpha$ .

Let us first define the notation  $H(k, m) = (-1)^{k-m} \prod_{j=m}^k \frac{2j+1}{2j+2}$ . The relation between the potentials  $\Phi_{D_n}$  is

$$\Phi_{D_{n+1}} = \frac{2n+1}{\alpha^{2n+1}} \int_0^\alpha \hat{\alpha}^{2n} \Phi_{D_n}(R, 0; \hat{\alpha}) d\hat{\alpha}. \quad (1)$$

The representation of the potential  $\Phi_{D_n}$  for  $R \geq \alpha$  can be defined by

$$\Phi_{D_n} = -\frac{\pi G \sigma_0}{2\alpha^{2n-1}} \prod_{j=0}^{n-1} (2j+1) R^{2n} \left[ \sum_{k=0}^n b_{n,k} (\xi^2 - 1)^k \sin^{-1} \xi + \xi \sum_{k=0}^{n-1} c_{n,k} (\xi^2 - 1)^k \sqrt{1 - \xi^2} \right], \quad (2)$$

where the coefficients  $b_{n,k}$  and  $c_{n,k}$  are defined as

$$\begin{aligned}b_{n+1,k} &= \frac{b_{n,k-1}}{2k}, \text{ for } k = 1, 2, \dots, n+1, \\ b_{n+1,0} &= \left( \frac{b_{n,n}}{2n+2} + c_{n,n-1} \right) H(n, 0) + \sum_{k=1}^{n-1} \left( \frac{b_{n,k}}{2k+1} + c_{n,k} + c_{n,k-1} \right) H(k, 0) + \left( \frac{b_{n,0}}{4} + \frac{c_{n,0}}{2} \right), \\ c_{n+1,n} &= \left( \frac{b_{n,n}}{2n+2} + c_{n,n-1} \right) \frac{H(n, n)}{2n+1}, \\ c_{n+1,m} &= \left( \frac{b_{n,n}}{2n+2} + c_{n,n-1} \right) \frac{H(n, m)}{2m+1} + \sum_{k=m}^{n-1} \left( \frac{b_{n,k}}{2k+2} + c_{n,k} + c_{n,k-1} \right) \frac{H(k, m)}{2m+1},\end{aligned}$$

where  $m = 1, 2, \dots, n-1$  and

$$c_{n+1,0} = \left( \frac{b_{n,n}}{2n+2} + c_{n,n-1} \right) H(n, 0) + \sum_{k=1}^{n-1} \left( \frac{b_{n,k}}{2k+2} + c_{n,k} + c_{n,k-1} \right) H(k, 0) + \left( \frac{b_{n,0}}{4} + \frac{c_{n,0}}{2} \right),$$

with initial data  $b_{1,0} = 1$ ,  $b_{1,1} = 2$ , and  $c_{1,0} = 1$ , and

$$\Phi_{D_n} = -\frac{\pi^2 G \sigma_0}{4\alpha^{2n-1}} \prod_{j=0}^{n-1} (2j+1) R^{2n} \sum_{k=0}^n b_{n,k} (\xi^2 - 1)^k$$



for  $R \leq \alpha$ . The derivation is straight forward from (1) and (2) with the help of the following identities,

$$\begin{aligned}\int \xi(\xi^2 - 1)^k \sin^{-1} \xi d\xi &= \frac{1}{2k+2}(\xi^2 - 1)^{k+1} \sin^{-1} \xi + \frac{1}{2k+2} \int (\xi^2 - 1)^k \sqrt{1 - \xi^2} d\xi, \\ \int (\xi^2 - 1)^k \sqrt{1 - \xi^2} d\xi &= \sum_{m=0}^k \frac{H(k, m)}{2m+1} \xi(\xi^2 - 1)^m \sqrt{1 - \xi^2} + H(k, 0) \sin^{-1} \xi, \\ \int \sqrt{1 - \xi^2} d\xi &= \frac{1}{2} \xi \sqrt{1 - \xi^2} + \frac{1}{2} \sin^{-1} \xi.\end{aligned}$$

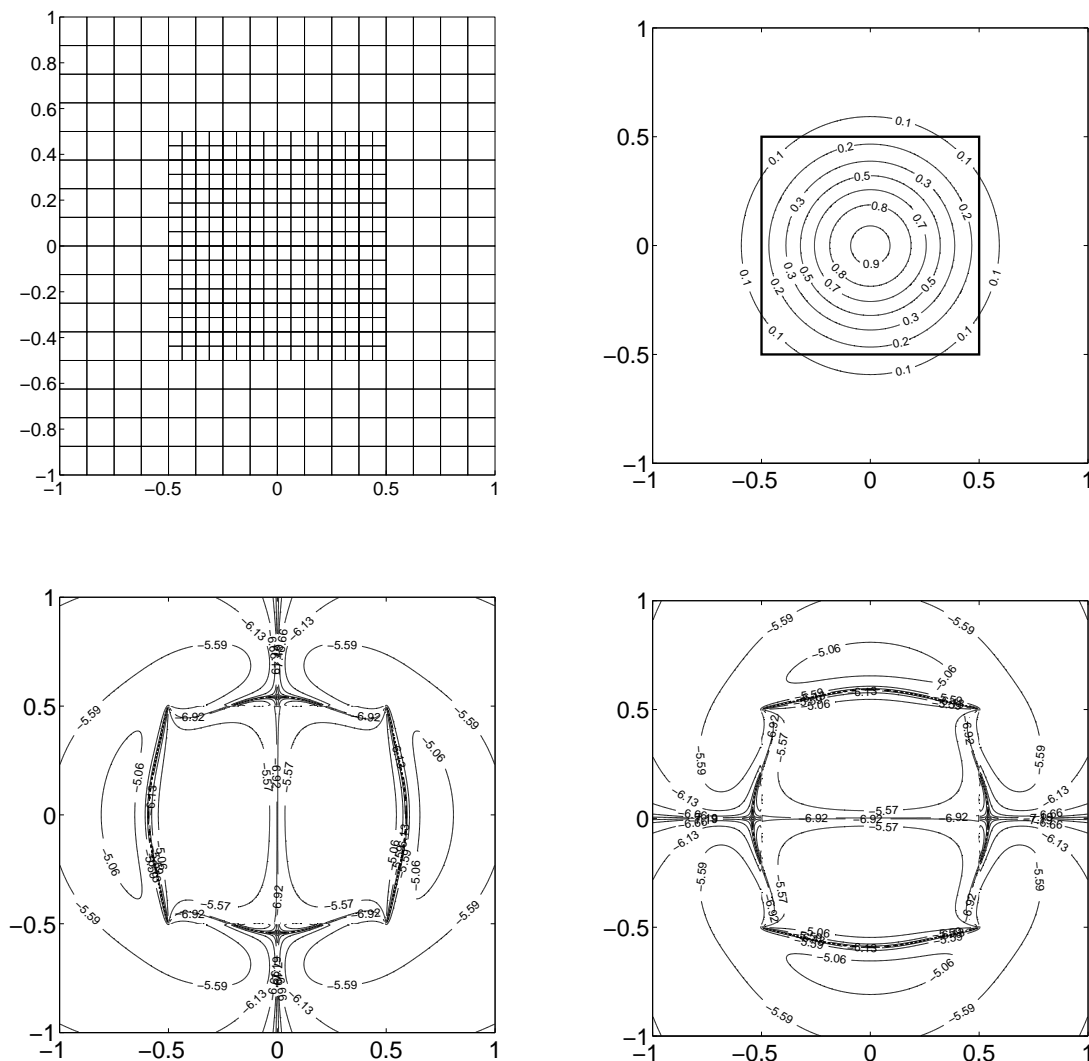


Fig. 1.— The numerical simulations of a  $\sigma_{D_5}$  disk for  $N = 512$  based on two grid levels. The relation between the coarser and finer grids is sketched in top-left panel. The contour plot in the top-right panel is the surface density. The square with thick line shows the boundary of the refined grid. The corresponding errors between the analytic and numerical solutions are shown for  $x$ -force (bottom-left) and  $y$ -force (bottom-right). The values in the contour plots in the bottom row are the absolute errors in the common logarithmic scale.

$N$	$E_x^1$	$E_x^2$	$E_x^\infty$	$E_R^1$	$E_R^2$	$L_R^\infty$
32	1.391E-3	2.232E-3	1.253E-2	2.198E-3	3.005E-3	1.253E-2
64	3.567E-4	5.292E-4	3.366E-3	5.668E-4	7.221E-4	3.359E-3
128	9.022E-5	1.275E-4	8.926E-4	1.435E-4	1.754E-4	8.914E-4
256	2.268E-5	3.114E-5	2.358E-4	3.606E-5	4.302E-5	2.355E-4
512	5.683E-6	7.675E-6	6.212E-5	9.037E-6	1.063E-5	6.202E-5
1024	1.423E-6	1.903E-6	1.633E-5	2.262E-6	2.639E-6	1.630E-5
$N$	$O_x^1$	$O_x^2$	$O_x^\infty$	$O_R^1$	$O_R^2$	$O_R^\infty$
32/64	1.96	2.08	1.90	1.95	2.06	1.90
64/128	1.98	2.05	1.91	1.98	2.04	1.91
128/256	1.99	2.03	1.92	1.99	2.03	1.92
256/512	2.00	2.02	1.92	2.00	2.02	1.92
512/1024	2.00	2.01	1.93	2.00	2.01	1.93

Table 1: Table demonstrating the errors and order accuracy for the  $\sigma_{D_5}$  disk for various number of zones  $N = 2^k$  of the finer grids from  $k = 5$  to 10 for the two grid level simulation. It shows that the order for the  $\sigma_{D_5}$  disk is almost second order for each norm.

$N$	$E_x^1$	$E_x^2$	$E_x^\infty$	$E_R^1$	$E_R^2$	$L_R^\infty$
32	8.632E-4	1.600E-3	1.194E-2	1.311E-3	2.109E-3	1.194E-2
64	2.206E-4	3.666E-4	3.226E-3	3.393E-4	4.902E-4	3.218E-3
128	5.552E-5	8.612E-5	8.581E-4	8.570E-5	1.162E-4	8.567E-4
256	1.391E-5	2.067E-5	2.272E-4	2.149E-5	2.806E-5	2.269E-4
512	3.481E-6	5.038E-6	6.000E-5	5.380E-6	6.862E-6	5.989E-5
1024	8.707E-7	1.241E-6	1.580E-5	1.346E-6	1.693E-6	1.577E-5
$N$	$O_x^1$	$O_x^2$	$O_x^\infty$	$O_R^1$	$O_R^2$	$O_R^\infty$
32/64	1.97	2.13	1.89	1.95	2.11	1.89
64/128	1.99	2.09	1.91	1.99	2.08	1.91
128/256	2.00	2.06	1.92	2.00	2.05	1.92
256/512	2.00	2.04	1.92	2.00	2.03	1.92
512/1024	2.00	2.02	1.92	2.00	2.02	1.93

Table 2: Table demonstrating the errors and order accuracy for the  $\sigma_{D_5}$  disk for various number of zones  $N = 2^k$  of the finer grids from  $k = 5$  to 10 for a three grid level simulation. It shows that the order for the  $\sigma_{D_5}$  disk is almost second order for each norm.

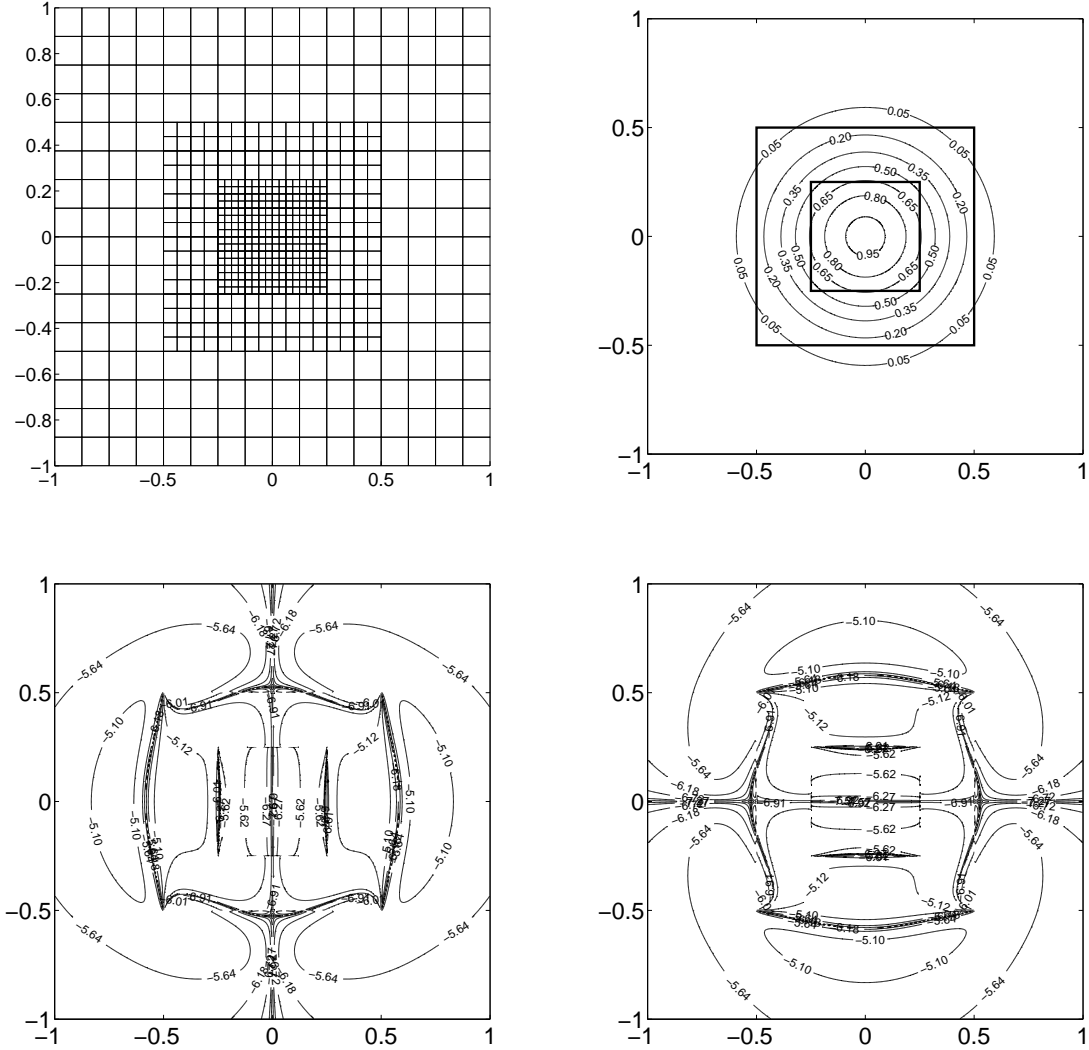


Fig. 2.— The numerical simulations of a  $\sigma_{D_5}$  disk for  $N = 512$  based on three grid levels,  $\ell = 0, 1, 2$ . The relation among the grid levels is sketched in top-left panel. The contour plot in the top-right panel is the surface density. The squares with thick line show the boundaries of the refined grids. The corresponding errors between the analytic and numerical solutions are shown for  $x$ -force (bottom-left) and  $y$ -force (bottom-right). The values in the contour plots in the bottom row are the absolute errors in the common logarithmic scale.

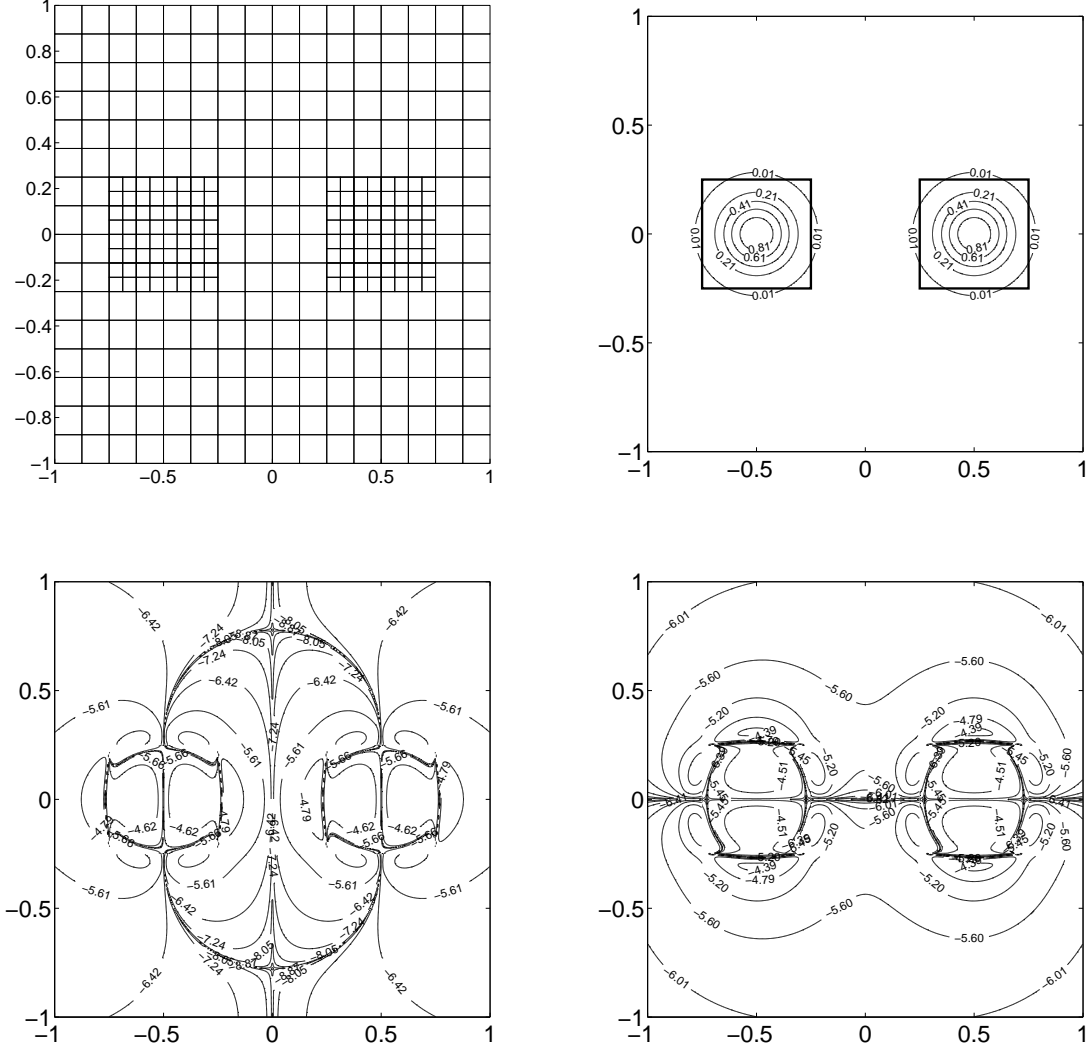


Fig. 3.— The numerical simulations of a non-axisymmetric case which consists of two  $\sigma_{D_5}$  disks with  $\alpha = \sqrt{2}/4$  and centers at  $(-1/2, 0)$  and  $(1/2, 0)$  for  $N = 512$  based on two grid levels. The relation between the coarser and finer grids is sketched in top-left panel. The contour plot in the top-right panel is the surface density. The squares with thick line show the boundaries of the refined grids. The corresponding errors between the analytic and numerical solutions are shown for  $x$ -force (bottom-left) and  $y$ -force (bottom-right). The values in the contour plots in the bottom row are the absolute errors in the common logarithmic scale.

$N$	$E_x^1$	$E_x^2$	$E_x^\infty$	$E_y^1$	$E_y^2$	$E_y^\infty$
32	3.200E-3	7.782E-3	4.830E-2	3.347E-3	7.751E-3	4.789E-2
64	7.854E-4	1.707E-3	1.340E-2	8.235E-4	1.702E-3	1.330E-2
128	1.993E-4	4.086E-4	3.647E-3	2.090E-4	4.075E-4	3.621E-3
256	5.065E-5	9.975E-5	9.874E-4	5.310E-5	9.951E-5	9.810E-4
512	1.277E-5	2.454E-5	2.666E-4	1.338E-5	2.449E-5	2.650E-4
1024	3.206E-6	6.072E-6	7.170E-5	3.359E-6	6.059E-6	7.129E-5
$N$	$O_x^1$	$O_x^2$	$O_x^\infty$	$O_y^1$	$O_y^2$	$O_y^\infty$
32/64	2.03	2.19	1.85	2.02	2.19	1.85
64/128	1.98	2.06	1.88	1.98	2.06	1.88
128/256	1.98	2.03	1.88	1.98	2.03	1.88
256/512	1.99	2.02	1.89	1.99	2.02	1.89
512/1024	1.99	2.02	1.89	1.99	2.02	1.89

Table 3: Table demonstrating the errors and order accuracy for the non-axisymmetric case, which consists of two  $\sigma_{D_5}$  disks with  $\alpha = \sqrt{2}/4$  and centers at  $(-1/2, 0)$  and  $(1/2, 0)$  for various number of zones  $N = 2^k$  of the finer grids from  $k = 5$  to 10 for a two grid level simulation. It shows that the order of accuracy is 2 for  $L^1$  and  $L^2$  norms, while 1.9 for  $L^\infty$  norm.

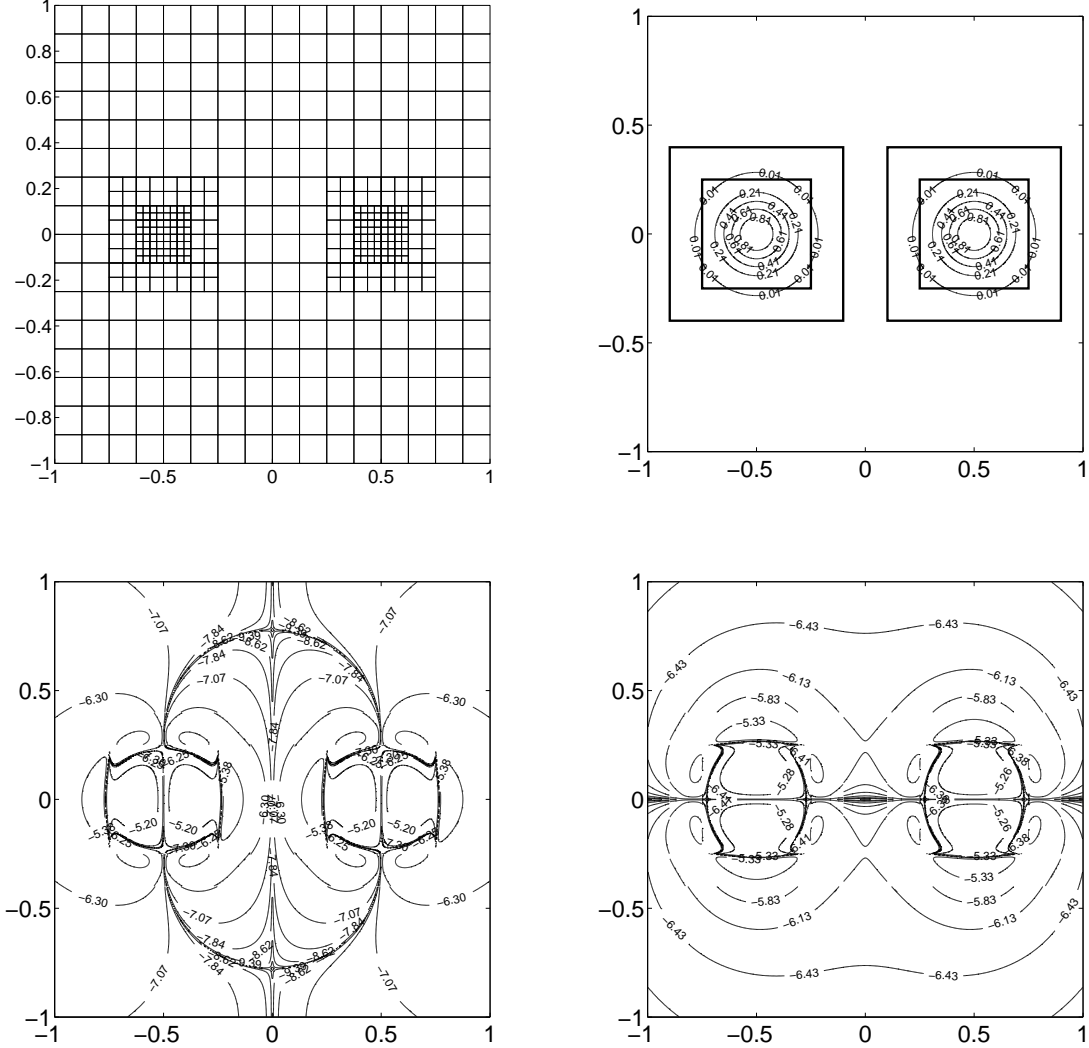


Fig. 4.— The numerical simulations of a non-axisymmetric case which consists of two  $\sigma_{D_5}$  disk with  $\alpha = \sqrt{2}/4$  and centers at  $(-1/2, 0)$  and  $(1/2, 0)$  for  $N = 512$  based on three grid levels,  $\ell = 0, 1, 2$ . The relation among the grid levels is sketched in top-left panel. The contour plot in the top-right panel is the surface density. The squares with thick line show the boundaries of the refined grids. The corresponding errors between the analytic and numerical solutions are shown for  $x$ -force (bottom-left) and  $y$ -force (bottom-right). The values in the contour plots in the bottom row are the absolute errors in the common logarithmic scale.

$N$	$E_x^1$	$E_x^2$	$E_x^\infty$	$E_y^1$	$E_y^2$	$E_y^\infty$
32	1.243E-3	2.186E-3	1.340E-2	1.257E-3	2.176E-3	1.330E-2
64	3.161E-4	5.233E-4	3.647E-3	3.202E-4	5.212E-4	3.621E-3
128	7.780E-5	1.251E-4	9.875E-4	7.892E-5	1.247E-4	9.810E-4
256	1.962E-5	3.079E-5	2.666E-4	1.991E-5	3.069E-5	2.650E-4
512	4.970E-6	7.657E-6	7.170E-5	5.039E-6	7.631E-6	7.129E-5
1024	1.245E-6	1.901E-6	1.921E-5	1.262E-6	1.895E-6	1.911E-5
$N$	$O_x^1$	$O_x^2$	$O_x^\infty$	$O_y^1$	$O_y^2$	$O_y^\infty$
32/64	1.97	2.06	1.88	1.97	2.06	1.88
64/128	2.02	2.06	1.88	2.02	2.06	1.88
128/256	1.99	2.02	1.89	1.99	2.02	1.89
256/512	1.98	2.01	1.89	1.98	2.01	1.89
512/1024	2.00	2.01	1.90	2.00	2.01	1.90

Table 4: Table demonstrating the errors and order accuracy for the non-axisymmetric case, which consists of two  $\sigma_{D_5}$  disks with  $\alpha = \sqrt{2}/4$  for various number of zones  $N = 2^k$  of the finer grids from  $k = 5$  to 10 for two grid level simulation. It shows that the order of accuracy is 2 for  $L^1$  and  $L^2$  norms, while 1.9 for  $L^\infty$  norm.

$N$	$E_x^1$	$E_x^2$	$E_x^\infty$	$E_R^1$	$E_R^2$	$L_R^\infty$
32	1.841E-3	3.495E-3	3.003E-2	2.799E-3	4.718E-3	2.847E-2
64	4.558E-4	9.025E-4	9.752E-3	6.967E-4	1.228E-3	9.179E-3
128	1.208E-4	2.528E-4	3.762E-3	1.848E-4	3.468E-4	3.756E-3
256	3.056E-5	6.321E-5	1.272E-3	4.661E-5	8.672E-5	1.250E-3
512	7.786E-6	1.705E-5	4.434E-4	1.187E-5	2.348E-5	4.409E-4
1024	1.951E-6	4.450E-6	1.531E-4	2.973E-6	6.143E-6	1.516E-4
$N$	$O_x^1$	$O_x^2$	$O_x^\infty$	$O_R^1$	$O_R^2$	$O_R^\infty$
32/64	1.99	1.95	1.62	2.00	1.94	1.63
64/128	1.92	1.84	1.37	1.92	1.82	1.29
128/256	1.98	2.00	1.56	1.99	2.00	1.59
256/512	1.97	1.89	1.52	1.97	1.89	1.50
512/1024	2.00	1.94	1.53	2.00	1.93	1.54

Table 5: Table demonstrating the errors and order accuracy for the  $\sigma_{D_2}$  disk for various number of zones  $N = 2^k$  of the finer grids from  $k = 5$  to 10 for the two grid level simulation. It shows that the order for the  $\sigma_{D_2}$  disk is almost second order in terms of  $L^1$  and  $L^2$  norms, while reduces to  $\approx 1.5$  for  $L^\infty$  norm.